



# Vacancy formation energies and migration barriers in multi-principal element alloys

Ankit Roy<sup>a,b,\*</sup>, Prashant Singh<sup>b</sup>, Ganesh Balasubramanian<sup>a</sup>, Duane D. Johnson<sup>b,c</sup>

<sup>a</sup> Department of Mechanical Engineering and Mechanics, Lehigh University, Bethlehem, PA 18015, USA

<sup>b</sup> United States Department of Energy, Ames Laboratory, Iowa State University, Ames, IA 50011, USA

<sup>c</sup> Department of Materials Science & Engineering, Iowa State University, Ames, IA 50011, USA



## ARTICLE INFO

### Article history:

Received 23 October 2021

Accepted 29 December 2021

Available online 5 January 2022

### Keywords:

Multi-principal element alloys

DFT

Vacancy defects

Vacancy stability

Vacancy diffusion

## ABSTRACT

Multi-principal element alloys (MPEAs) continue to garner interest as structural and plasma-facing materials due to their structural (phase) stability and increased resistance to radiation damage. Despite sensitivity of mechanical behavior to irradiation and point-defect formation, there has been scant attention on understanding vacancy stability and diffusion in refractory-based MPEAs. Using density-functional theory, we examine vacancy stability and diffusion barriers in body-centered cubic  $(\text{Mo}_{0.95}\text{W}_{0.05})_{0.85}\text{Ta}_{0.10}(\text{TiZr})_{0.05}$ . The results in this MPEA show strong dependence on environment, originating from local lattice distortion associated with charge-transfer between neighboring atoms that vary with different chemical environments. We find a correlation between degree of lattice distortion and migration barrier: (Ti, Zr) with less distortion have lower barriers, while (Mo, W) with larger distortion have higher barriers, depending up local environments. Under irradiation, our findings suggest that (Ti, Zr) are significantly more likely to diffuse than (Mo, W) while Ta shows intermediate effect. As such, material degradation caused by vacancy diffusion can be controlled by tuning composition of alloying elements to enhance creep strength at extreme operating temperatures and harsh conditions.

© 2022 Acta Materialia Inc. Published by Elsevier Ltd. All rights reserved.

## 1. Introduction

Power-generation plants, both thermal and nuclear, now demand novel structural and coating materials that retain excellent mechanical properties and stability even at elevated temperatures (>1000 °C). This quest for higher operating temperatures has led to a surge in research on complex alloys to achieve higher efficiency in power-generation technologies [1]. With this as motivation, the concept of multi-principal element alloys (MPEAs) was introduced by Yeh et al. [2] and Cantor et al. [3], with high-entropy alloys limited to near-equiatomic compositions. MPEAs have created a global revolution in alloy design never witnessed in past metallurgical research [2–5]. MPEAs were originally defined as having five or more elements in relatively high concentrations (5–35%). To enhance mechanical properties like hardness and elastic modulus at elevated temperatures [2,6–8], the principle was to add more elements and to maximize the configurational entropy to favor formation of simpler single-phase alloys [2,9]. But,

in the past several years, research on metastable MPEAs has revealed many alloys violate this principle [10–12]. Hence, the goal shifted towards developing alloys that may not contain as many elements in equal proportions, but rather a complex mix in an optimized fashion to obtain the best properties [4,13], including medium-entropy (3 or 4 elements) alloys. In the quest for promising compositions, experiments alone would do very little to explore the enormous search space with several billion MPEAs [14]. More recently, density-functional theory (DFT) [10,14] or molecular dynamics (MD) [15–17] methods combined with machine-learning [7,8,18,19] techniques played a key role in accelerating the discovery of promising MPEAs.

Currently, tungsten (W) is the leading candidate for plasma-facing components (PFCs) owing to its high melting temperature of 3422 °C, high thermal conductivity, low tritium retention, and low sputtering-erosion rates in cold scrape-off layer plasma [20,21]. Despite its widespread application in PFCs, tungsten has limitations like poor fracture toughness, high brittle-to-ductile transition temperature, and a risk of forming nanoscale bubbles under irradiation by He ions [22] restricting its use in fusion reactors. As such, one alternative route is by tuning MPEA properties for applications where good irradiation resistance is required. In fact, recent experimental efforts have revealed certain body-centered cubic (bcc)

\* Corresponding author at: Department of Mechanical Engineering and Mechanics, Lehigh University, Bethlehem, PA 18015, USA.

E-mail addresses: [ankitroy@alum.lehigh.edu](mailto:ankitroy@alum.lehigh.edu) (A. Roy), [psingh84@ameslab.gov](mailto:psingh84@ameslab.gov) (P. Singh).

alloys like  $W_{38}Ta_{36}Cr_{15}V_{11}$  show no trace of dislocation loops created during irradiation up to a dose of 8 displacements-per-atom (dpa) [23]. Unlike as observed in pure W, the mobility of self-interstitials and vacancies is similar and there is a large imbalance in defect mobility [24,25]. Apart from excellent irradiation resistance, refractory-based MPEAs with bcc phase exhibit superior high-temperature mechanical properties over existing alloys [6]. Notably, unlike face-centered-cubic (fcc) MPEAs, bcc alloys do not exhibit radiation-hardening [26]. These findings are attributed to the distribution of point defects caused by high-energy ion bombardment. Therefore, it is of fundamental interest to understand the defect-related properties of MPEAs, such as vacancy stability and vacancy diffusion, especially their control.

Here we analyze defect properties of a refractory-based bcc MPEA, specifically we focus on  $(Mo_{0.95}W_{0.05})_{0.85}Ta_{0.10}(TiZr)_{0.05}$  (denoted as MWTTZ), reported to exhibit  $3\times$  higher room-temperature elastic moduli [13] and superior oxidation resistance [27]. The high-temperature Young's modulus of MWTTZ ( $\sim 2\times$  at 2000 K relative to commercial alloys like TZM, composed of Ti-Zr-Mo) makes it an interesting alloy for in-depth analysis. The vacancy formation energy and migration energy barriers were calculated and their trends are presented. Our findings reveal that Ti has the lowest-energy migration barrier whereas W has the highest. We also find that local lattice distortions (LLD) caused by atomic displacements from their ideal alloy (x-ray average lattice) positions are directly proportional to the charge transfers between the neighboring atoms, impacting barrier energies. These revelations prove critical towards understanding the resistance to radiation damage of refractory-based bcc MPEAs.

## 2. Computational methods

### 2.1. Density-functional theory (DFT)

We employed first-principles DFT as implemented in the Vienna *Ab-initio* Simulation Package (VASP) to investigate the effect of vacancies on structural and electronic properties of MWTTZ [28,29]. To represent the disordered MPEA configuration, we used a Supercell Random Approximate (SCRAP) [33] optimized to get atomic point and pair correlation functions (3 to 5 neighbor shells) considering three different supercell sizes (80, 120, and 160 atoms). The vacancy formation energy convergence with SCRAPs size in MWTTZ was used as a criterion to choose optimal (most computationally efficient) unit-cell size to get reliable results. As expected, these differently sized SCRAPs had no effect on the elemental vacancy formation energies ( $E_{form}^{vac}$ ) [33]. For pure elements, 54-atom bcc (Mo/W/Ta) and hcp (Ti/Zr) supercells were used to simulate  $E_{form}^{vac}$ . A gamma-centered Monkhorst-Pack [30] *k*-mesh of  $1 \times 2 \times 2$  ( $3 \times 4 \times 4$ ) was used for bcc Brillouin-zone integration during geometry optimization (charge self-consistency). A kinetic-energy cutoff of 520 eV was used both for total energy ( $10^{-5}$  eV/cell) and force ( $-0.001$  eV/Å) convergence. The Perdew, Burke and Ernzerhof (PBE) exchange-correlation for solids was used [31,32].

### 2.2. Vacancy-formation energy ( $E_{form}^{vac}$ )

$E_{form}^{vac}$  in the MPEA was estimated by

$$E_{form}^{vac} = E_v - E_0 \pm \mu_v, \quad (1)$$

where  $E_v$  is the energy with the vacancy,  $E_0$  is the energy without the vacancy and  $\mu_v$  is the chemical potential of the defect species  $v$ , where the + sign (− sign) corresponds to a vacancy (interstitial) [34].

**Table 1**

Percentage chemical potential difference ( $\Delta\mu_{Elements} = \mu_{alloy} - \mu_{metal}$ ) of alloying elements in alloys and pure metals [34–36].

Sl. No.	Refs.	Metals	% $\Delta\mu$
1	[34]	V, Ta, Cr, W	1.28
2	[35]	Cr, Mn, Fe, Co	1.24
3	[36]	Ni, Co, Cr, Fe	3.04

**Table 2**

Comparison of elemental chemical potentials ( $\mu_v$ ) in pure metal and bcc MWTTZ.

Element	Phase (VEC)	$\mu_v$	$\mu_{v/alloy}$
		[eV-atom <sup>-1</sup> ]	
Ti	hcp (4)	−8.10	−8.08
Zr	hcp (4)	−8.52	−8.51
Ta	bcc (5)	−11.81	−11.70
Mo	bcc (6)	−10.80	−10.71
W	bcc (6)	−12.96	−12.82

### 2.3. Chemical potential ( $\mu_v$ )

The  $\mu_v$  is defined as energy variation when one atom is added or removed from the system. In the solid-state, it is usually calculated as energy-per-atom of the corresponding element. Although the definition of  $\mu_v$  remains the same in complex alloys, the values can be different from that of pure metals. However, in the literature, the variation of  $\mu_v$  in pure metals (bulk) versus in an alloy were found to be insignificant [34,35], as shown in Table 1. This suggests that, in most cases, taking elemental  $\mu_v$  as starting point may save significant computational effort.

Nevertheless, we reinvestigate the variation of  $\mu_v$  in MPEAs [37] using relationship between elemental and alloy  $\mu_v$  as

$$\mu_v + \sum_{i \neq v} c_i \mu_{eff}^v = \mu_{v/alloy}, \quad (2)$$

where  $\mu_{v/alloy}$  is the chemical potential of metal  $v$  when present in the alloy,  $i$  refers to the site of the vacancy. The  $\mu_{eff}^v$  can be calculated using  $\mu_{eff}^v = \frac{\Delta E_0}{\Delta C_v}$ , where  $\Delta E_0 (= E_v - E_0)$  refers to the energy difference per atom between the systems with and without a vacancy, and  $\Delta C_v$  is the concentration change of the element  $v$  with the finite-sized ( $N$  site) supercell in the vacancy and no vacancy cases ( $\frac{1}{N-1} - \frac{1}{N} = \frac{1}{N(N-1)}$ ). The calculated values of  $\mu_{eff}^v$  are listed in Table 2. Note that Eq. (2) reduces to  $\mu_v = \mu_{v/alloy} = E_{alloy}/N$  for a pure metal, as  $\sum_{i \neq v} c_i \mu_{eff}^v = 0$  when there is only a single species in the system. In Table 2, the difference between  $\mu_v$  and  $\mu_{v/alloy}$  is less than 1.1%, which matches recent reports; for instance, here  $\mu_{v/alloy}$  for Ta is  $-11.70$  eV-atom<sup>-1</sup> in agreement with  $-11.72$  eV-atom<sup>-1</sup> [34]. Thus,  $\mu_{v/alloy}$  in Table 2 was used throughout this work.

### 2.4. Migration-energy barrier

The energy barrier for defect migration was calculated using the climbing-image nudged-elastic band (cNEB) methodology [38]. The cNEB scheme generates the minimum energy path for the defect migration, which was calculated by generating multiple atomic configurations along a linear path that has negligible or no atomic forces normal to it. We used 6 intermediate atomic configurations to calculate the migration barrier. From the energies of each of those individual atomic configurations and subsequently from the energy profile of the migration path, the mechanism of the plausible defect migration and its energy barrier was calculated. This information is significant as it provides an insight into the kinetics of defect progression and also the mechanisms that possibly lead to defect recovery [39].

**Table 3**

DFT-calculated  $E_{form}^{Vac}$  in pure metals are compared with those obtained via specific heat or spectroscopy measurements [42–44]. A percent change was given by (Expt. – DFT)  $\times$  100/DFT.

Metal atoms	$E_{form}^{Vac}$ (eV/atom)		% Change
	DFT (this work)	Expt.	
W	3.26	3.30 [41]	1.2
Mo	2.87	3.00 [41]	4.3
Ta	2.90	3.10 [42]	6.5
Zr	2.00	1.75 [43]	14.3
Ti	2.07	1.55 [41]	33.6

### 3. Results and discussions

#### 3.1. Vacancy-formation energies of pure metals

Point defects are defined as imperfections in the crystal lattice with sizes of the order of the atomic diameter. The enthalpy of formation ( $E_{form}$ ) is a characteristic of vacancies that governs the equilibrium concentration at any given temperature. The  $E_{form}$  of interstitials is higher than that of the vacancy defects, therefore, vacancies naturally become the dominating defect type at equilibrium [40]. Experimentally,  $E_{form}^{Vac}$  is the energy required to remove one atom from the interior of the crystal and replace it on the crystal surface [40]. The equilibrium concentration of point defects (both vacancy and interstitials) increases with temperature, which can be calculated by measuring specific heat, thermal expansion, electrical resistivity, positron annihilation, thermopower and perturbed angular correlation of  $\gamma$ -quanta [40]. Information on causes of discrepancies between  $E_{form}^{Vac}$  from various measurement methods relevant to this work is provided in the supplementary materials. In Table 3, we compare DFT calculated  $E_{form}^{Vac}$  of metal atoms with experimental values (obtained via specific heat measurements and positron annihilation spectroscopy) [41]. This shows less than 6.5% difference for bcc elements, while a large deviation was found for hcp elemental metals. The observed discrepancy is attributed to experimental techniques, for example, the  $E_{form}^{Vac}$  values via specific heat or by positron annihilation spectroscopy lead to completely different results [40].

The  $E_{form}^{Vac}$  for Ti in Table 3 has been compared to the experimental value that was obtained by specific heat measurements [41]. In the supplement, we have highlighted the possible ways that can lead to inaccuracy in  $E_{form}^{Vac}$  during specific-heat measurements, i.e., the deviations with DFT  $E_{form}^{Vac}$  can be attributed to type of measurements. To understand this further, we designed multiple vacancy configurations in a 54-atom supercell to calculate the  $E_{form}^{Vac}$  to replicate the experimental scenario. We designed 6 atomic configurations with a 13.94 Å vacuum included in each configuration to avoid interactions among periodic images of both vacancy and surface-surface layers. Our strategy covers all possible scenarios of vacancy formation by removing atoms from 6 different positions in the supercell representing a solid, as shown in Fig. S1. The vacancy created at surface layer by removing the atom to infinity in Fig. S1f most closely matches with the experiments. But this process does not reflect the mechanism of vacancy formation (removal of an interior atom from crystal associated with the appearance of an atom on crystal surface). The removal of an atom, one atom at a time from the surface to vacuum, is the representation of the adatom binding energy [44]. Such an analysis is useful to study the energetic criteria for adsorption of an organic molecules on metal surfaces, which was recently used to facilitate user-defined vacancy patterning by the adsorption of  $C_{60}$  molecules on gold, aluminum and beryllium surfaces [44] for applications in biosensors [45] and optoelectronics [46]. However, the  $E_{form}^{Vac}$  calculated

**Table 4**

$E_{form}^{Vac}$  of each alloying element of MWTTZ compared to pure-metal value, with percent change calculated as  $[E_{form, alloy}^{Vac} - E_{form, v}^{Vac}] \times 100 / E_{form, v}^{Vac}$ .

Element	$E_{form, alloy}^{Vac}$ [eV]		$E_{form, v}^{Vac}$ [eV] Pure metal	% Change	
	Env#1	Env#2		Env#1	Env#2
W	3.49	3.07	3.26	7.1	–5.8
Ta	3.79	3.71	2.90	30.7	27.9
Mo	3.84	3.57	2.87	33.8	24.4
Zr	2.87	3.23	2.00	43.5	61.5
Ti	3.62	3.42	2.07	74.9	65.2

using the conventional approach is the main focus of this work, where an atom was extracted from the bulk to create the vacancy defects [34,35,47].

#### 3.2. MPEA vacancy-formation energies

$E_{form}^{Vac}$  of each element in MWTTZ are listed in Table 2. The elemental chemical potentials in Table 2 were used to estimate  $E_{form}^{Vac}$  using Eq. (1). In Table 4,  $E_{form}^{Vac}$  shows a wide range from 2.87 eV for  $V_{Zr}$  to 3.84 eV for  $V_{Mo}$ , similar to other reports [36,48]. The energy spread of 0.97 eV can potentially be attributed to the considerable LLD. The  $E_{form}^{Vac, alloy}$  shows increase with respect to  $E_{form}^{Vac, v}$  with variation from 7% to 74%, where  $V_W$  shows an increase of 7% while Ti is 74%. Tungsten with the highest melting point (3422 °C) undergoes the least change in  $E_{form}^{Vac}$ , which comes from stronger metallic bonding as W has a larger valence-electron count (VEC=6) than Ti/Zr (VEC=4) and Ta (VEC=5). A similar effect was observed for Mo (VEC=6). On the other hand,  $V_{Ti}$  shows maximum increase in  $E_{form}^{Vac}$  compared to the hcp Ti vacancy, where the metallic bonds are weaker, as reflected in its lowest melting point of 1668 °C. We also show a chemical environment dependence of  $E_{form}^{Vac}$  in Table 4, where  $V_W$  shows 6% drop compared to the pure metal, while all other elements show significant increase.

Thermodynamic properties depend strongly on the local chemical environment and atomic interaction [33], even more critical for non-stoichiometric cases as the unit-cell are more complex depending on composition. Therefore, it is wise to explore the effect of SCRAP size on  $E_{form}^{Vac}$  of MWTTZ before going into more detail. In Fig. 1, we plot  $E_{form}^{Vac}$  for each alloying element calculated in three different sizes of SCRAPs with 80, 120 and 160 atoms. Our calculations show a considerable increase in  $E_{form}^{Vac}$  from 0.1 to 0.5 eV/atom, however, these effects diminish for 120 and 160 atom SCRAPs. This suggests that careful evaluation of size effect is important in MPEAs, especially for non-stoichiometric compositions. More importantly, having large enough cell is critical to avoid interaction of vacancy or defects with its periodic images. Therefore, the SCRAP size was chosen such that the image distance between successive vacancies remains at a minimum of 12 Å. Hence, a 160-atom SCRAP was used in all vacancy-related calculations to avoid numerical issues and size-dependent effects.

#### 3.3. Local lattice distortions

Solid-solution strengthening leads to improved mechanical properties of refractory MPEAs, which is often attributed to LLD driven by chemical complexity of alloying [49–51]. However, we find no reports on how point-defects impact LLD and any mechanism that can control this behavior. Fig. 2 shows the vector displacements of the first-nearest neighbors (NN) in environment 1 (Fig. 2a,b) and second-NN in environment 2 (Fig. 2c,d) for a Ti vacancy compared to no-vacancy case. Environment 1 and 2 indicate different positions in the lattice where a specific metal vacancy

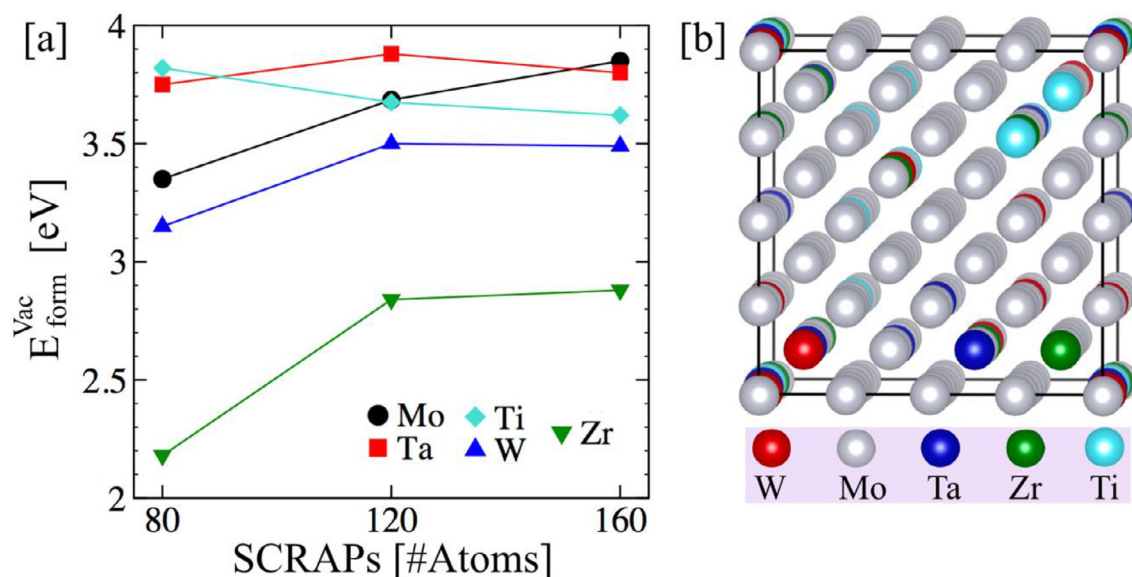


**Fig. 1.** In MWTTZ, (a) dependence on SCRAP size for  $E_{\text{form}}^{\text{Vac}}$  for each element. A considerable change in  $E_{\text{form}}^{\text{Vac}}$  was found for W/Mo/Zr with increasing cell size. (b) Schematic of 160-atom (4 × 4 × 5 × 2-atom bcc cell) SCRAP used in this work for off-stoichiometric MPEAs.

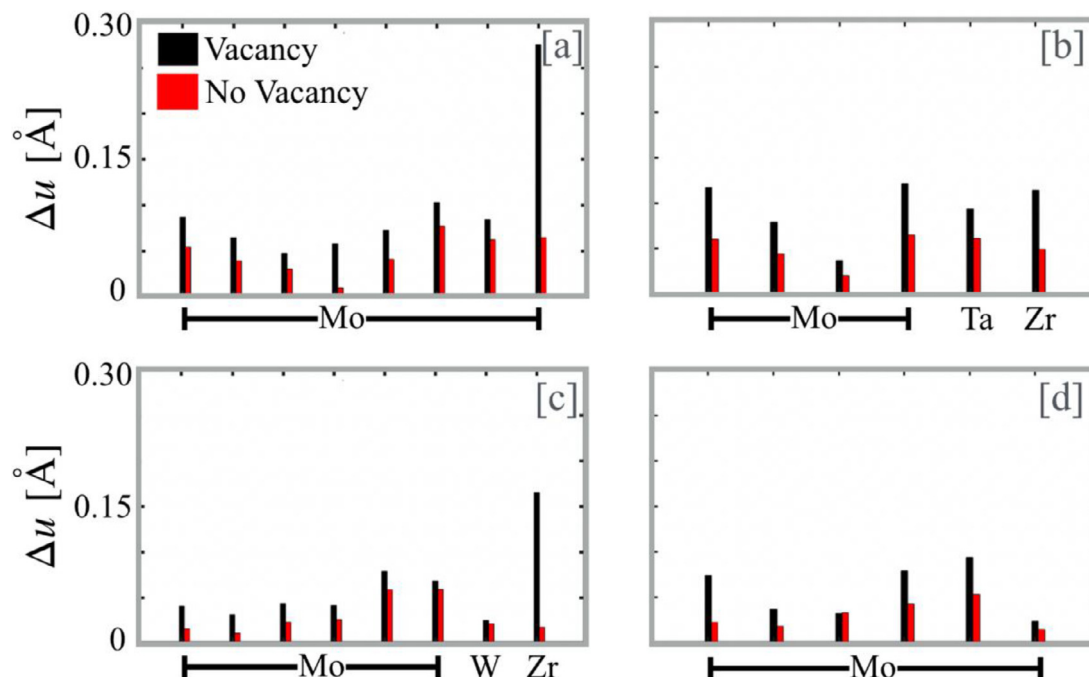


**Fig. 2.** Vector atomic displacements in MWTTZ of (a, c) first-, and (b, d) second-nearest neighbor environment around a Ti vacancy (black bars) compared to no-vacancy case (red bars) (For interpretation of the references to color in this figure legend, the reader is referred to the web version of this article).

was created by removing a metal atom. A Zr atom in the 1<sup>st</sup> NN in both the environments undergoes a large distortion in the presence of a vacancy, which occurs due to a charge deficiency (vacancy) created by the missing Ti atom and, as such, the Zr atom readjusts itself with the neighboring atoms to compensate for that deficiency. Atomic displacements near vacancy sites are larger due to a need of increased charge readjustment caused by the vacancy. The observation that unlike-atom species in the NN cause higher displacements of NNs is consistent through all metal vacancies. The vector atomic displacements from  $V_{\text{Mo}}/V_{\text{Ta}}/V_{\text{W}}/V_{\text{Zr}}$  are shown in the supplementary Fig. S2–S5.

Recently, Song et al. [49] have shown that hard-sphere model ( $\delta$  size-difference parameter [52]) fails to estimate the LLD ac-

curately, e.g., it overestimates in refractory MPEAs and underestimates in 3d MPEAs. So, to avoid using empirical estimates, we explored the quantum-mechanical origin of LLD through DFT calculated charge density analysis. Atoms in complex MPEAs with diverse chemical environment can lead to varying degree of interaction resulting from strong charge fluctuation among unlike-metal-atom pairs with differing electronegativities. We hypothesize a significant charge transfer between unlike species, resulting in larger atomic displacements from their ideal lattice (average x-ray) positions. In Fig. 3, charge-density differences ( $\Delta\rho = \rho_{\text{vac}} - \rho_{\text{no-vac}}$ ) are plotted with and without vacancy, where the charge readjustments of no-vacancy case (colored blue) are compared to vacancy cases (colored yellow) at various metal sites.

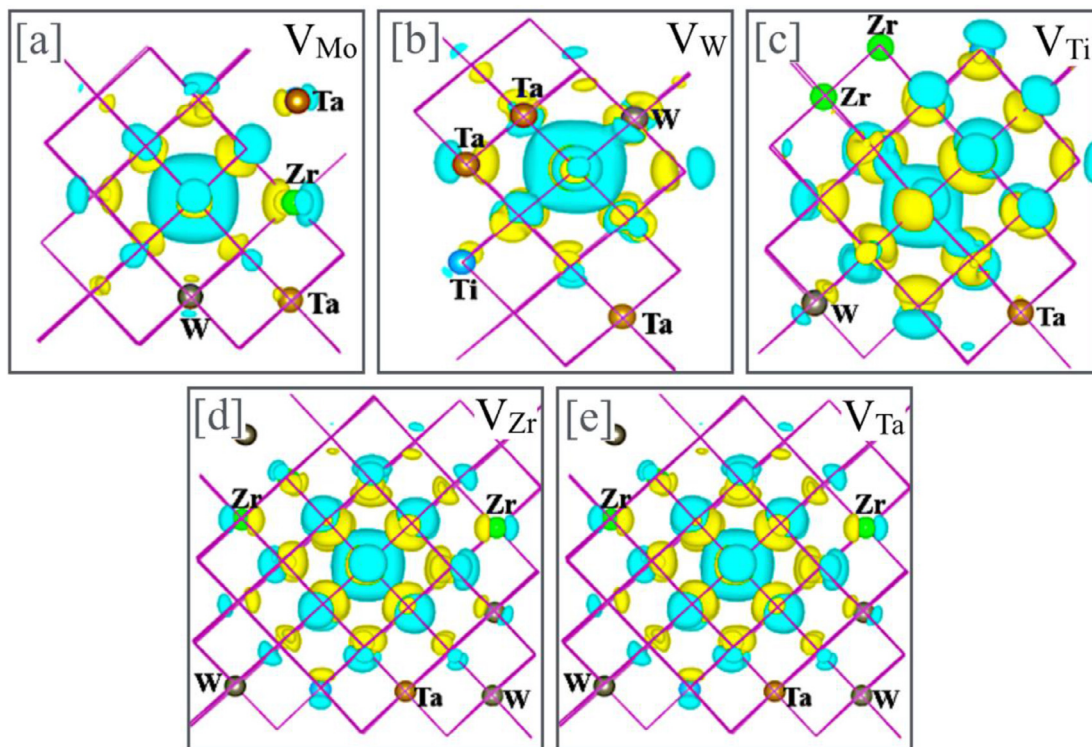


**Fig. 3.** Charge-density difference ( $\Delta\rho = \rho_{vac} - \rho_{no-vac}$ ) in MWTTZ between no-vacancy and vacancy cases of (a)  $V_{Mo}$ , (b)  $V_W$ , (c)  $V_{Ti}$ , (d)  $V_{Zr}$  and (e)  $V_{Ta}$ . Effect of  $V_{Zr}$  on charge redistribution in (c) was strongest (out to 5<sup>th</sup> NNs) and correlated with Zr being the least electronegative among all elements (For interpretation of the references to color in this figure, the reader is referred to the web version of this article).

In Fig. 3a, the charge redistribution ( $\Delta\rho$ ) is more localized (2<sup>nd</sup> NNs) for  $V_{Mo}$ . This localized  $\Delta\rho$  due to weaker effect of charge-transfer with 1<sup>st</sup> and 2<sup>nd</sup> NNs is expected to have no significant effect on the LLD arising from local chemical environment in MWTTZ. As Mo and W have same VEC with similar atomic sizes, the same effect on  $\Delta\rho$  was observed for  $V_W$  in Fig. 3b. Thus,  $V_W$  is expected to have a similar effect on LLD as  $V_{Mo}$ . Contrastingly,  $V_{Ti}$  and  $V_{Zr}$  show local lattice relaxation effect up to 4<sup>th</sup> and 5<sup>th</sup> NNs, respectively, due to charge redistribution. This occurs likely due to large charge-variation introduced by Ti and Zr vacancies, as is obvious in Fig. 3c,d, where  $\Delta\rho$  is beyond 2<sup>nd</sup> NNs [34,53]. The  $V_{Ta}$  (group V, VEC=5) in Fig. 3e shows  $\Delta\rho$  behavior intermediate to  $V_{Mo}/V_W$  (group VI, VEC=5) and  $V_{Ti}/V_{Zr}$  (group IV, VEC=4) as its VEC is intermediate. This behavior is explained via electronegativity difference ( $\Delta\chi$ ), where atoms with higher  $\chi$  should pull more charge than atoms with lower  $\chi$ . If Fig. 3a,e is analyzed based on electronegativities, then Zr ( $\chi = 1.33$ ), Ti ( $\chi = 1.54$ ) and Ta ( $\chi = 1.50$ ) in a mostly Mo-rich environment show more delocalized charges from 3<sup>rd</sup> to 5<sup>th</sup> NNs while elements with higher electronegativity, i.e., Mo ( $\chi = 2.16$ ) < W ( $\chi = 2.36$ ), show more localized charges due to higher electron affinity.

In Fig. 3, a vacancy causes a varying degree of electron transfer depending on atom type, so a varying strength of metallic bonds should be expected. The qualitative quantum-mechanical insights in Fig. 3 show the mechanism controlling atomic displacements before and after creation of a vacancy. Such a mechanism has been previously noted to induce LLD [34,47], but we provide more quantitative inference in Fig. 4 by plotting net-displacement in 1<sup>st</sup>-NN atom versus charge transfer. The net displacement is defined as the difference with respect to ideal bcc as  $\sqrt{(x_1 - x)^2 + (y_1 - y)^2 + (z_1 - z)^2}$  (with no-vacancy lattices ( $x, y, z$ ) vs. vacancy ( $x_1, y_1, z_1$ )), and  $\Delta\rho$  is the difference between vacancy and no-vacancy cases.

As discussed in Fig. 3, charge redistribution is explained through the ordering of elemental electronegativity. The quantitative analysis of charge transfer in Fig. 4a,e shows that Ti (1.54), Zr (1.33) and Ta (1.5) tend to undergo the maximum redistribution of charges in the range 0.13–0.17  $e^-/\text{\AA}^3$ . In contrast, Mo (2.16)/W(2.36) with higher electronegativity shows charge transfer in the similar range, i.e., 0.08  $e^-/\text{\AA}^3$ . Despite great variance, each metal vacancy shows a near linear trend of atomic displacements versus charge transfer, where Ti, Zr and Ta show highest displacements owing to the maximum degree of charge transfer.

In the 160-atom SCRAP (128 Mo sites), inclusion of other neighbors than Mo may result in more outliers owing to other atomic properties like atomic mass and radius in charge analysis. Therefore, for consistency, the displacement versus charge-transfer plotted in Fig. 4a,e includes only Mo atoms as the 1<sup>st</sup> NN. We observed that electronic rearrangement increased the metallic character around vacancy sites, where sites with large charge fluctuation show increased atomic displacement from ideal sites that directly relates to LLD. The increased LLD makes it difficult to move or extract an atom out of the lattice and increases  $E_{form}^{vac}$ , as shown in Table 4.

The presence of certain outliers in Fig. 4a,e is conjectured to show up in cases where the 2<sup>nd</sup> NNs has some role in charge transfer. For instance, for the  $V_W$  in Fig. 4b, the displacement of one of the surrounding Mo atoms breaks from linearity. On the other hand, the presence of Zr in the 2<sup>nd</sup> NNs (see Fig. S5) displaces the Mo atom due to a large electronegativity difference between the Zr (1.33) and Mo (2.16). Similarly, Zr in the 2<sup>nd</sup> NNs in  $V_{Mo}$  case shows fewer outliers.

### 3.4. Vacancy-migration energies

Vacancies are the most common type of point defects at equilibrium and they largely control the diffusion kinetics. At ele-

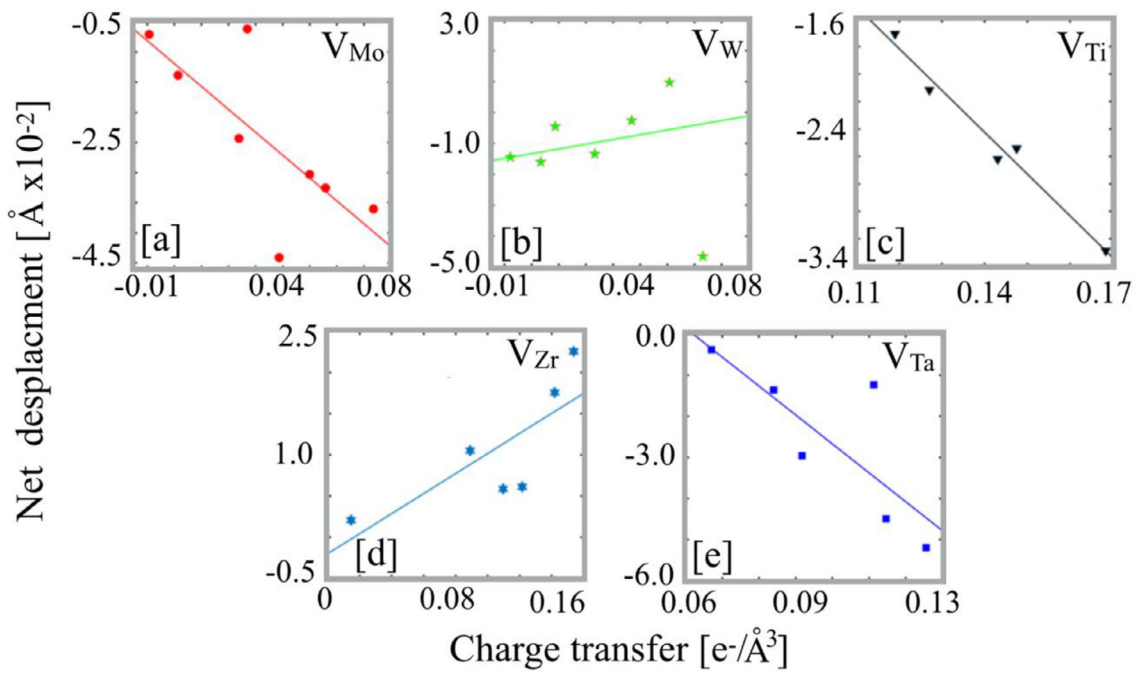


**Fig. 4.** Correlation between charge-transfer ( $e^-/\text{\AA}^3$ ) and net-displacement in MWTTZ at Mo sites in the first-neighbors for (a)  $V_{\text{Mo}}$ , (b)  $V_{\text{W}}$ , (c)  $V_{\text{Ti}}$ , (d)  $V_{\text{Zr}}$  and (e)  $V_{\text{Ta}}$  vacancies with respect to no-vacancy case. For simplicity, only Mo NNs around the vacancy sites were considered in the charge analysis.

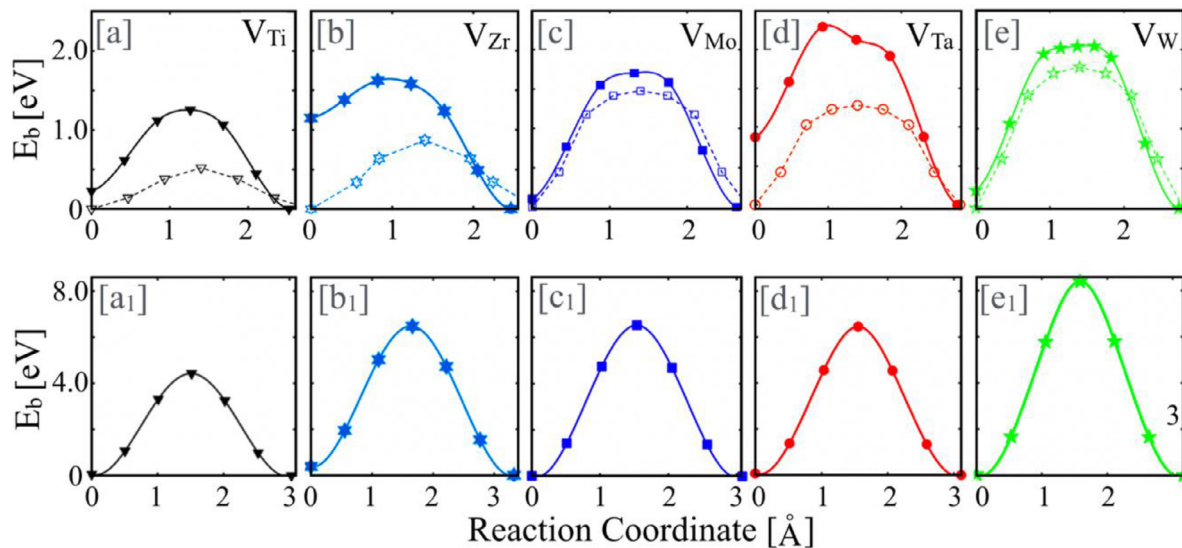


**Fig. 5.** Calculated vacancy-migration energy and barriers ( $E_b$ ) for MWTTZ along (a-e)  $\frac{1}{2}$  111 direction (solid lines) compared to barriers of pure metals (dashed lines), and (a<sub>1</sub>-e<sub>1</sub>) along 100 direction. Pure metal  $E_b$  are from Ref. [55] ( $V_{\text{Ti}}$ ), Ref. [56] ( $V_{\text{Zr}}$ ), and Ref. [57] ( $V_{\text{Mo}}$ ,  $V_{\text{Ta}}$ , and  $V_{\text{W}}$ ). Migration energies appear to increase with group number from periodic table.

vated temperatures, vacancy diffusion becomes a critical aspect as the vacancy migration controls the chemistry driven transformations, for example corrosion and creep [54]. To date, few studies have been done to explore the vacancy-diffusion mechanism in refractory-based bcc MPEAs [34]. In Fig. 5a-e, we analyzed vacancy migration barriers in disordered MWTTZ and compare to those of pure metals [55-58].

We used cNEB to calculate migration barriers in MWTTZ. cNEB generates a sequence of atomic configurations and provides an information for warping of the migration path (i.e., “elastic band”) with a goal to move towards a low-energy path in the landscape of potential-energy surface. The diffusion barriers for vacancies in the alloy versus pure metals are shown in Fig. 5a-e, where energy barriers in alloy matrix (solid lines) are compared to those in

pure metals (dashed lines) [51-53]. The energy barrier in the alloy for  $V_{\text{Ti}}/V_{\text{Zr}}$  shows significant increase. This was explained through the charge-density readjustment (electronegativities) caused by vacancies in different chemical environments (Fig. 3) that leads to significant increase in  $E_{\text{form}}^{\text{vac}}$  of  $V_{\text{Ti}}/V_{\text{Zr}}$  compared to  $V_{\text{Mo}}/V_{\text{W}}/V_{\text{Ta}}$ , as listed in Table 3. We attribute this fact to the larger readjustment of charges up to 5th-nearest neighbors for hcp metal vacancies ( $V_{\text{Ti}}/V_{\text{Zr}}$ ) compared to bcc metal vacancies, i.e., increased interaction among the Zr neighbors. Interestingly,  $V_{\text{Ti}}/V_{\text{Zr}}$  also show anisotropic charge distribution that points towards strong environment dependence, also visible in migration barrier of  $V_{\text{Zr}}$  in Fig. 5b. This phenomenon can also be understood in terms of pair distribution function that shows increased interatomic interactions between unlike atomic pairs in Fig. S6 as compared to the interaction

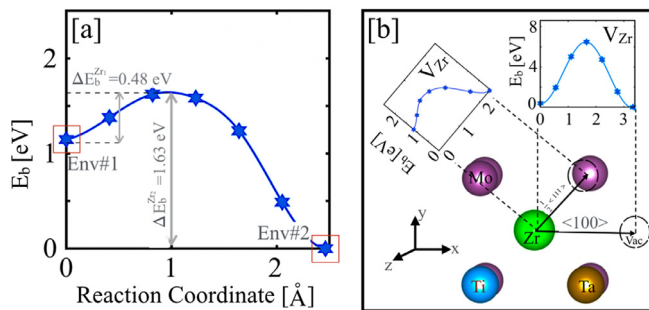


**Fig. 6.** (a) Environmental and (b) directional dependence of migration energy barrier for  $V_{Zr}$  in MWTTZ. Migration barrier in  $\langle 100 \rangle$  is higher by a factor of 2, 3 over  $\frac{1}{2}\langle 111 \rangle$  due to lower close-packing in  $\langle 100 \rangle$  plane, i.e., low linear density. A significant variation in migration barrier (environment 1  $\Delta E_b^{Zr1} = 0.48$  eV and environment 2  $\Delta E_b^{Zr2} = 1.63$  eV) suggests that vacancies created in environment 2 may remain intact through the irradiation exposure period but those in environment 1 are more likely to undergo diffusion.

between like pairs in MWTTZ. Similar behavior has been reported previously [15], where the pair-correlation function [ $g_{\alpha\beta}(r)$ ] of unlike pairs was found to have a higher interaction than like pairs. For example, Ta-Ta pairs in Fig. S6 are weaker than the Ta-Mo, Ta-Zr and Ta-W, which further affirms our hypothesis. Hence, when metal elements crystallize in an alloy, the migration of an atom to a neighboring vacancy site becomes formidable due to the strong interaction arising from the diverse environment, which depends on type of neighbor as well as diversity of neighbors.

The magnitude of electronegativity ( $\chi$ ) represents the ability of element to attract the charge, i.e., higher  $\chi$  indicates higher affinity to pull charge. In the increasing order,  $\chi$  of each alloying elements is Zr (1.33) < Ta (1.50) < Ti (1.54) < Mo (2.16) < W (2.36). Higher  $\chi$  would mean a larger  $\Delta\chi$  and larger charge exchange with NNs, therefore, a stronger interaction. This makes the complex concentrated alloy unfavorable for vacancy diffusion. Hence, we anticipate that the order of migration barriers should be proportional to the  $\chi$  of elements. If we closely look at migration barriers in Fig. 5, indeed, the migration barrier of each element falls in the same order as their  $\chi$  with the exception of Ti. A lower atomic mass of Ti may override the  $\chi$  contribution, where the lowest atomic mass allows a higher vibrational frequency and velocity at a given temperature compared to other elements, perhaps playing a role in lowering the diffusion barrier of Ti.

We also investigated the directional dependence of migration barrier in MWTTZ. The  $\frac{1}{2}\langle 111 \rangle$  Burger's vector in [110] plane in Fig. 5a–e shows 2–3 times lower barriers compared to  $\langle 100 \rangle$  in [100] plane in Fig. 5a<sub>1</sub>–e<sub>1</sub>. Notably, the  $\langle 111 \rangle$  direction lies in close-packed [110] bcc plane, which has higher packing fraction (higher atomic density). Therefore, the energy required to move vacancy on a close-packed plane under external force will be relatively smaller than the less closed-packed [100] direction, where the atoms have lower atomic density.

Diffusion energetics in Fig. 5 shows that Ti is relatively favorable compared to Zr/Ta and Mo/W and will assist the diffusion. Therefore, to emphasize on element specific diffusion, we discuss the environment dependence of migration barrier in MWTTZ. The barrier heights for all metals in MPEA show dependence on local environment, especially  $V_{Zr}$  and  $V_{Mo}$ . We discuss the case of  $V_{Zr}$  (Fig. 6) as it shows the maximum variation in diffusion barrier with change in local environment. Fig. 6a and b show environment and directional dependence, respectively. We observed a considerable disparity in migration barrier depending upon the local environment (Fig. 6a), where  $\Delta E_b^{Zr1} = 0.48$  eV in environment 1 while  $\Delta E_b^{Zr2} = 1.63$  eV in environment 2. Experimentally, a higher diffusion barrier for  $V_{Zr}$  in environment 2 (with its larger charge

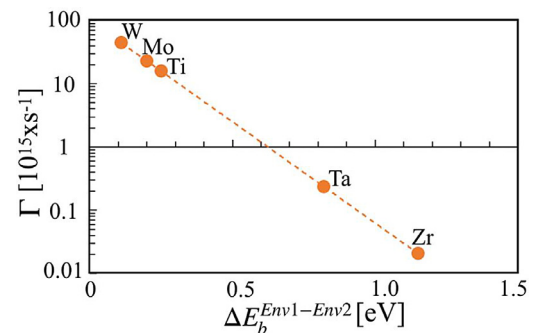


**Fig. 7.** Defect jump-rate ( $\Gamma$ ) plot on logarithmic scale in MWTTZ. The order of jump-rate shows strong correlation with difference of diffusion barrier of defects in two different environments in Fig. 5.

redistribution near  $V_{Zr}$  site than in environment 1) indicates that vacancies are difficult to move, i.e., a significant fraction of the vacancies, once created, will remain intact during the irradiation process, but those in environment 1 should more easily diffuse.

**Jump Frequency:** Here we present a mean-field-like understanding of one-dimensional jump frequency of constituent elements of MWTTZ. The defect jump rate can be described in terms of the Arrhenius relation [59,60], which can be defined as

$$\Gamma = \nu e^{-E_b/k_B T}, \quad (3)$$

where  $E_b$  is the energy barrier required to move defect to the saddle point from an equilibrium position,  $k_B$  is Boltzmann's constant,  $T$  is absolute temperature (Kelvin), and  $\nu$  is the vibrational frequency of defect along the saddle point. The results in Fig. 7 show that  $\Gamma$  in the disordered MWTTZ is strongly correlated with the migration barrier, as shown in Fig. 5. The defect jump rate to its original position is of the order of  $\Gamma(W) > \Gamma(Mo) > \Gamma(Ti) > \Gamma(Ta) > \Gamma(Zr)$ . This important finding indicates that an atom jumping to the defect site interacts with the surrounding atoms, which can greatly impact the atomic diffusion in the solid-solution phase. The defect-atom interaction in varying degree of environment in MPEAs are greatly impacted by the probability of a defect's jump.

#### 4. Conclusions

We investigated the environment dependence of the vacancy-formation energy  $E_{form}^{Vac}$  and associated diffusion barrier in  $(Mo_{0.95}W_{0.05})_{0.85}Ta_{0.10}(TiZr)_{0.05}$ , a refractory-based bcc MPEA. The  $E_{form}^{Vac}$  of metal atoms in this MPEA was found to increase from 7% for W to 74% for Ti compared to the pure metals. The higher  $E_{form}^{Vac}$  of Ti suggests that a Ti vacancy is hard to create, however, a low diffusion barrier for Ti indicates that once a Ti vacancy is formed, its migration becomes relatively easier compared to other atom types. The charge-transfer effect (governed by electronegativities) establishes that LLD in MPEAs has a quantum origin that can be tuned through controlled variation of local atomic environments. We exemplified this with DFT atomic displacements versus local environments with and without a vacancy and showed that displacements greatly vary with type of metal-vacancy and its local environments. Indeed, the atomic displacement showed approximately linear dependence on the net charge transfer.

We also calculated migration-energy barrier ( $E_b^{Vac}$ ) for vacancy atoms in this refractory MPEA. The  $E_b^{Vac}$  are significantly higher for Ti and Mo than pure-metal state, while other metal atoms show very weak dependence. Importantly, the large  $E_b^{Vac}$  in the MPEA was attributed to stronger unlike pair interactions that make migration difficult.  $E_b^{Vac}$  also shows direct correlation with electronegativity, where higher electronegative atoms show higher barriers.

The migration-energy barriers show a strong environmental and directional dependence. For example, the barriers for  $V_{Zr}$ ,  $\Delta E_b^{Zr}$  varied by a factor of 3 (0.48 eV to 1.63 eV) depending on local starting environment; and, for directional dependence,  $V_{Zr}$  shows a factor of 2–3 times higher  $E_b^{Vac}$  along  $\langle 100 \rangle$  direction than  $\frac{1}{2} \langle 111 \rangle$  direction due to lower packing fraction making diffusion difficult in bcc alloys. Atomic displacements provided a strong correlation between charge redistribution, LLD, and chemical environment for unique insight into point-defect properties in refractory MPEAs. For defect formation and migration, this study provides chemical insights to manipulate and improve the high-temperature thermo-mechanical properties of refractory MPEAs, especially for use in extreme environments, affected by vacancy formation and diffusion phenomena, like creep.

### Data availability

The authors declare that the data supporting the findings of this study are available within the paper and supplement. Also, the data that support the plots within this paper and other finding of this study are available from the corresponding author upon reasonable request.

### Declaration of Competing Interest

The authors declare that they have no known competing financial interests or personal relationships that could have appeared to influence the work reported in this paper.

### CRediT authorship contribution statement

**Ankit Roy:** Methodology, Writing – original draft, Writing – review & editing. **Prashant Singh:** Conceptualization, Supervision, Formal analysis, Writing – original draft, Writing – review & editing. **Ganesh Balasubramanian:** Funding acquisition, Supervision, Resources, Writing – review & editing. **Duane D. Johnson:** Conceptualization, Formal analysis, Funding acquisition, Supervision, Resources, Writing – review & editing.

### Acknowledgments

Ankit Roy, while visiting Ames Laboratory, was supported in part by the [National Science Foundation](#) (NSF) through award [CMMI-1944040](#). General theory developments at Ames Laboratory were supported by the Department of Energy (DOE), Office of Science, Basic Energy Sciences, Materials Science and Engineering Department. Ames Laboratory is operated by [Iowa State University](#) for the U.S. DOE under contract [DE-AC02-07CH11358](#). Specific theory application to MWTTZ was supported by the U.S. DOE, Office of Energy Efficiency and Renewable Energy, Advanced Manufacturing Office (AMO) project WBS 2.1.0.19.

### Supplementary materials

Supplementary material associated with this article can be found, in the online version, at doi:[10.1016/j.actamat.2021.117611](https://doi.org/10.1016/j.actamat.2021.117611).

### References

- [1] S. Carnot, *Reflections on the Motive Power of Heat and on Machines Fitted to Develop that Power*, John Wiley, 1890.
- [2] J.W. Yeh, S.K. Chen, S.J. Lin, J.Y. Gan, T.S. Chin, T.T. Shun, C.H. Tsau, S.Y. Chang, Nanostructured high-entropy alloys with multiple principal elements: novel alloy design concepts and outcomes, *Adv. Eng. Mater.* 6 (2004) 299–303.
- [3] B. Cantor, I.T.H. Chang, P. Knight, A.J.B. Vincent, Microstructural development in equiatomic multicomponent alloys, *Mater. Sci. Eng. A Struct.* 375 (2004) 213–218.
- [4] E.P. George, W. Curtin, C.C. Taran, High entropy alloys: a focused review of mechanical properties and deformation mechanisms, *Acta Mater.* 188 (2020) 435–474.
- [5] D.B. Miracle, O.N. Senkov, A critical review of high entropy alloys and related concepts, *Acta Mater.* 122 (2017) 448–511.
- [6] O.N. Senkov, G.B. Wilks, J.M. Scott, D.B. Miracle, Mechanical properties of  $Nb_{25}Mo_{25}Ta_{25}W_{25}$  and  $V_{20}Nb_{20}Mo_{20}Ta_{20}W_{20}$  refractory high entropy alloys, *Intermetallics* 19 (2011) 698–706.
- [7] A. Roy, T. Babuska, B. Krick, G. Balasubramanian, Machine learned feature identification for predicting phase and Young's modulus of low-, medium- and high-entropy alloys, *Scr. Mater.* 185 (2020) 152–158.
- [8] J.M. Rickman, H.M. Chan, M.P. Harmer, J.A. Smeltzer, C.J. Marvel, A. Roy, G. Balasubramanian, Materials informatics for the screening of multi-principal elements and high-entropy alloys, *Nat. Commun.* 10 (2019) 2618.
- [9] M.H. Tsai, J.W. Yeh, High-entropy alloys: a critical review, *Mater. Res. Lett.* 2 (2014) 107–123.
- [10] A. Roy, P. Sreeramagiri, T. Babuska, B. Krick, P.K. Ray, G. Balasubramanian, Lattice distortion as an estimator of solid solution strengthening in high-entropy alloys, *Mater. Charact.* 172 (2021) 110877.
- [11] Z. Wu, H. Bei, G.M. Pharr, E.P. George, Temperature dependence of the mechanical properties of equiatomic solid solution alloys with face-centered cubic crystal structures, *Acta Mater.* 81 (2014) 428–441.
- [12] M. Gianelle, A. Kundu, K. Anderson, A. Roy, G. Balasubramanian, H.M. Chan, A novel ceramic derived processing route for multi-principal element alloys, *Mater. Sci. Eng. A* 793 (2020) 139892.
- [13] P. Singh, A. Sharma, A.V. Smirnov, M.S. Djalilo, P.K. Ray, G. Balasubramanian, D.D. Johnson, Design of high-strength refractory complex solid-solution alloys, *npj Comput. Mater.* 4 (2018) 16.
- [14] D. Miracle, High entropy alloys as a bold step forward in alloy development, *Nat. Commun.* 10 (2019) 1–3.
- [15] A. Roy, J. Munshi, G. Balasubramanian, Low energy atomic traps sluggish the diffusion in compositionally complex refractory alloys, *Intermetallics* 131 (2021) 107106.
- [16] Q. Ding, Y. Zhang, X. Chen, X. Fu, D. Chen, S. Chen, L. Gu, F. Wei, H. Bei, Y. Gao, Tuning element distribution, structure and properties by composition in high-entropy alloys, *Nature* 574 (2019) 223–227.
- [17] P. Sreeramagiri, A. Roy, G. Balasubramanian, Effect of cooling rate on the phase formation of AlCoCrFeNi high-entropy alloy, *J. Phase Equilibria Diffus.* 42(5) (2021) 772–780 (2021).
- [18] A. Roy, G. Balasubramanian, Predictive descriptors in machine learning and data-enabled explorations of high-entropy alloys, *Comput. Mater. Sci.* 193 (2021) 110381.
- [19] T. Kostuchenko, F. Körmann, J. Neugebauer, A. Shapeev, Impact of lattice relaxations on phase transitions in a high-entropy alloy studied by machine-learning potentials, *npj Comput. Mater.* 5 (2019) 1–7.
- [20] S.J. Zinkle, J.T. Busby, Structural materials for fission & fusion energy, *Mater. Today* 12 (2009) 12–19.
- [21] V. Philippis, Tungsten as material for plasma-facing components in fusion devices, *J. Nucl. Mater.* 415 (2011) S2–S9.
- [22] J. Marian, C.S. Becquart, C. Domain, S.L. Dudarev, M.R. Gilbert, R.J. Kurtz, D.R. Mason, K. Nordlund, A.E. Sand, L.L. Snead, Recent advances in modeling and simulation of the exposure and response of tungsten to fusion energy conditions, *Nucl. Fusion* 57 (2017) 092008.
- [23] O. El-Atwani, N. Li, M. Li, A. Devaraj, J. Baldwin, M.M. Schneider, D. Sobieraj, J.S. Wróbel, D. Nguyen-Manh, S.A. Maloy, Outstanding radiation resistance of tungsten-based high-entropy alloys, *Sci. Adv.* 5 (2019) eaav2002.
- [24] C. Becquart, C. Domain, Modeling microstructure and irradiation effects, *Metall. Mater. Trans. A* 42 (2011) 852–870.
- [25] T. Suzudo, M. Yamaguchi, A. Hasegawa, Stability and mobility of rhenium and osmium in tungsten: first principles study, *Model. Simul. Mater. Sci. Eng.* 22 (2014) 075006.
- [26] Y. Lu, H. Huang, X. Gao, C. Ren, J. Gao, H. Zhang, S. Zheng, Q. Jin, Y. Zhao, C. Lu, A promising new class of irradiation tolerant materials:  $Ti_2ZrHf_{0.5}Mo_{0.2}$  high-entropy alloy, *J. Mater. Sci. Technol.* 35 (2019) 369–373.
- [27] R. Su, H. Zhang, G. Ouyang, L. Liu, W. Nachlas, J. Cui, D.D. Johnson, J.H. Perepezko, Enhanced oxidation resistance of  $(Mo_{95}W_5)_{85}Ta_{10}$  (TiZr)<sub>5</sub> refractory multi-principal element alloy up to 1300°C, *Acta Mater.* 215 (2021) 117114.
- [28] G. Kresse, D. Joubert, From ultrasoft pseudopotentials to the projector augmented-wave method, *Phys. Rev. B* 59 (1999) 1758.
- [29] G. Kresse, J. Hafner, Ab initio molecular dynamics for liquid metals, *Phys. Rev. B* 47 (1993) 558.
- [30] H.J. Monkhorst, J.D. Pack, Special points for Brillouin-zone integrations, *Phys. Rev. B* 13 (1976) 5188.
- [31] P.E. Blöchl, Projector augmented-wave method, *Phys. Rev. B* 50 (1994) 17953.
- [32] J.P. Perdew, K. Burke, M. Ernzerhof, Generalized gradient approximation made simple, *Phys. Rev. Lett.* 77 (1996) 3865.
- [33] R. Singh, A. Sharma, P. Singh, G. Balasubramanian, D.D. Johnson, Accelerating computational modeling and design of high-entropy alloys, *Nat. Comput. Sci.* 1 (2021) 54–61.
- [34] S. Zhao, Defect properties in a VTaCrW equiatomic high entropy alloy (HEA) with the body centered cubic (bcc) structure, *J. Mater. Sci. Technol.* 44 (2020) 133–139.
- [35] M. Mizuno, K. Sugita, H. Araki, Defect energetics for diffusion in CrMnFeCoNi high-entropy alloy from first-principles calculations, *Comput. Mater. Sci.* 170 (2019) 109163.

- [36] S. Zhao, T. Egami, G.M. Stocks, Y. Zhang, Effect of d electrons on defect properties in equiatomic NiCoCr and NiCoFeCr concentrated solid solution alloys, *Phys. Rev. Mater.* 2 (2018) 013602.
- [37] A. Esfandiarpour, M. Nasrabadi, Vacancy formation energy in CuNiCo equimolar alloy and CuNiCoFe high entropy alloy: ab initio based study, *Calphad* 66 (2019) 101634.
- [38] G. Henkelman, B.P. Uberuaga, H. Jónsson, A climbing image nudged elastic band method for finding saddle points and minimum energy paths, *J. Chem. Phys.* 113 (2000) 9901–9904.
- [39] S. Middleburgh, R. Grimes, Defects and transport processes in beryllium, *Acta Mater.* 59 (2011) 7095–7103.
- [40] Y. Kraftmakher, Equilibrium vacancies and thermophysical properties of metals, *Phys. Rep.* 299 (1998) 79–188.
- [41] B. Medasani, M. Haranczyk, A. Canning, M. Asta, Vacancy formation energies in metals: a comparison of MetaGGA with LDA and GGA exchange–correlation functionals, *Comput. Mater. Sci.* 101 (2015) 96–107.
- [42] P. Jung, H. Ullmaier, Production of atomic defects in metals, in: Landolt-Börnstein, Group III: Crystal and Solid State Physics, Springer-Verlag, Berlin, 1991, p. 25.
- [43] G. Hood, R. Schultz, J. Jackman, Recovery of single crystal. cap alpha.-Zr from low temperature electron irradiation. A positron annihilation spectroscopy study, *J. Nucl. Mater.* 126 (1984) 126 (Netherlands).
- [44] A. Kaiser, F. Vines, F. Illas, M. Ritter, F. Hagelberg, M. Probst, Vacancy patterning and patterning vacancies: controlled self-assembly of fullerenes on metal surfaces, *Nanoscale* 6 (2014) 10850–10858.
- [45] K. Schierbaum, T. Weiss, E.T. Van Veizen, J. Engbersen, D. Reinhoudt, W. Göpel, Molecular recognition by self-assembled monolayers of cavitant receptors, *Science* 265 (1994) 1413–1415.
- [46] E. Menard, M.A. Meitl, Y. Sun, J.U. Park, D.J.L. Shir, Y.S. Nam, S. Jeon, J.A. Rogers, Micro-and nanopatterning techniques for organic electronic and optoelectronic systems, *Chem. Rev.* 107 (2007) 1117–1160.
- [47] P. Singh, D. Saucedo, R. Arroyave, The effect of chemical disorder on defect formation and migration in disordered max phases, *Acta Mater.* 184 (2020) 50–58.
- [48] C. Li, J. Yin, K. Odbadrakh, B.C. Sales, S.J. Zinkle, G.M. Stocks, B.D. Wirth, First principle study of magnetism and vacancy energetics in a near equimolar NiFeMnCr high entropy alloy, *J. Appl. Phys.* 125 (2019) 155103.
- [49] H. Song, F. Tian, Q.M. Hu, L. Vitos, Y. Wang, J. Shen, N. Chen, Local lattice distortion in high-entropy alloys, *Phys. Rev. Mater.* 1 (2017) 023404.
- [50] Y. Ikeda, K. Gubaev, J. Neugebauer, B. Grabowski, F. Körmann, Chemically induced local lattice distortions versus structural phase transformations in compositionally complex alloys, *npj Comput. Mater.* 7 (2021) 1–8.
- [51] H. Chen, A. Kauffmann, S. Laube, I.C. Choi, R. Schwaiger, Y. Huang, K. Lichtenberg, F. Müller, B. Gorr, H.J. Christ, Contribution of lattice distortion to solid solution strengthening in a series of refractory high entropy alloys, *Metall. Mater. Trans. A* 49 (2018) 772–781.
- [52] Y. Zhang, Y.J. Zhou, J.P. Lin, G.L. Chen, P.K. Liaw, Solid-solution phase formation rules for multi-component alloys, *Adv. Eng. Mater.* 10 (2008) 534–538.
- [53] M. Muzyk, D. Nguyen-Manh, K. Kurzydowski, N. Baluc, S. Dudarev, Phase stability, point defects, and elastic properties of W-V and W-Ta alloys, *Phys. Rev. B* 84 (2011) 104115.
- [54] T.K. Tsao, A.C. Yeh, C.M. Kuo, K. Kakehi, H. Murakami, J.W. Yeh, S.R. Jian, The high temperature tensile and creep behaviors of high entropy superalloy, *Sci. Rep.* 7 (2017) 1–9.
- [55] S. Shang, L. Hector, Y. Wang, Z. Liu, Anomalous energy pathway of vacancy migration and self-diffusion in hcp Ti, *Phys. Rev. B* 83 (2011) 224104.
- [56] Y.N. Osetsky, D. Bacon, N. De Diego, Anisotropy of point defect diffusion in alpha-zirconium, *Metall. Mater. Trans. A* 33 (2002) 777–782.
- [57] D. Nguyen-Manh, S. Dudarev, A. Horsfield, Systematic group-specific trends for point defects in bcc transition metals: an ab initio study, *J. Nucl. Mater.* 367 (2007) 257–262.
- [58] A. Seeger, The study of point defects in metals in thermal equilibrium. I. The equilibrium concentration of point defects, *Journal of Physics F: Metal Physics* 3 (2) (1973) 248.
- [59] D.A. Terentyev, L. Malerba, M. Hou, Dimensionality of interstitial cluster motion in bcc-Fe, *Phys. Rev. B* 75 (2007) 104108.
- [60] G.H. Vineyard, Frequency and isotope effects in solid state rate processes, *J. Phys. Chem.* 3 (1957) 121–127.